

Fracture behaviour of an anisotropic polygranular graphite (PGA)

M. Mostafavi^{a,*}, M.J.J. Schmidt^b, B.J. Marsden^b, T.J. Marrow^a

^a Department of Materials, University of Oxford, UK

^b Nuclear Graphite Research Group, School of Mechanical, Aerospace and Civil Engineering, The University of Manchester (Materials Performance Centre), UK

ARTICLE INFO

Article history:

Received 5 May 2012

Received in revised form

26 July 2012

Accepted 2 August 2012

Available online 10 August 2012

Keywords:

Nuclear graphite

Anisotropy

Fracture toughness

Digital image correlation

Finite element analysis

ABSTRACT

This paper reports a numerical and experimental study on the mechanical and fracture properties of an anisotropic polygranular graphite: extruded nuclear grade Pile Grade A (PGA). The dynamic elastic moduli and Poisson's ratios were measured by the ultrasonic method and the fracture toughness was investigated using compact tension (CT) specimens: both as a function of orientation relative to the material grain direction. Digital image correlation was applied to monitor the full displacement field of the surface of the CT specimens, allowing the propagating crack and the fracture process zone around the tip of the crack to be observed and quantified. Rising fracture resistance (*R*-curve) behaviour is observed before unstable fracture, commensurate with the observed fracture process zone. We show that to accurately obtain the fracture resistance, the material anisotropy must be properly accounted for. This is demonstrated by comparing the experimental data for specimen compliance with finite element simulations for isotropic and orthotropic material properties. Digital image correlation validated the crack dimensions that were obtained from specimen stiffness, which was dominated by the lower of the anisotropic elastic moduli for all orientations. The use of a numerical method to evaluate fracture resistance, based on the incremental work done with crack extension (after Turner and Kolednik) is shown to be not reliable when the crack extension increments are insufficiently small relative to the gradient of the fracture resistance curve. There is a significant difference between the fracture properties of PGA with respect to the extrusion direction; cracks propagating across the extrusion direction (i.e. against the grain direction) have a fracture resistance that is approximately 50% higher than that for cracks propagating in a plane containing the extrusion direction.

© 2012 Elsevier B.V. All rights reserved.

1. Introduction

Pile Grade A or PGA is a needle coke graphite used in all of the UK Magnox reactors and many research reactors. It was produced from petroleum reformer residue coke obtained from the Shell oil refinery at Pernis, Holland. Coal tar pitch, usually from the North Thames Gas Board at Eastham, was used as the binder. The graphite blocks were produced by an extrusion process, which tends to align the needle-like crystallites with their basal planes parallel to the extrusion direction [1].

Typical non-irradiated mechanical properties of PGA are given in Table 1. PGA Graphite, as an extruded material based on “needle” shaped coke, displays a substantial anisotropy along the grain/extrusion direction (“with grain” or WG) compared to across that orientation (“against grain” or AG). This anisotropy is shown in Table 1. The material displays variations both between and within production batches, the former largely due to variations in the binder and impregnation pitches employed [1].

The WG and AG definitions of direction are commonly used in the nuclear graphite community to define the anisotropy of properties such as strength and stiffness. However, engineering fracture mechanics employs a standardised notation for directions, as illustrated in Fig. 1 (e.g. [2]). This defines six orientations in which a compact tension specimen can be tested for an anisotropic material, described using the normal axis of the crack plane, and the through thickness direction of the specimen (i.e. the crack front direction, which is orthogonal to the crack propagation direction). These orientations, which take into account both the specimen and material directions are described with reference to the longitudinal (L), transverse (T) and short transverse (S) directions. The L direction is equivalent to the WG direction while the T and S directions are equally equivalent to the AG direction in an extruded material such as PGA. Hence, the six specimen orientations are reduced to three: in the first (TL or SL), the crack propagates along the grain orientation (i.e. in the WG direction); in second (ST or TS), the crack propagates across the grain orientation (i.e. in the AG direction) and the crack front is parallel to the AG direction; in the third (LS or LT) both the crack propagation direction and the crack front are against the grain. This terminology is summarised in Table 2 and the unique orientations TL, ST and LS are used throughout this paper. The ST and LS orientations examine the fracture of the same plane in the

* Corresponding to: Department of Materials, University of Oxford, Parks Road, Oxford OX1 3PH, UK. Fax: +44 1865 273789.

E-mail address: mahmoud.mostafavi@materials.ox.ac.uk (M. Mostafavi).

Nomenclature

a	crack length
da	crack growth
d	load line displacement
$f(a/W)$	geometry function
AG	“against grain” direction
A_0 – A_6	parameters in compliance expression
B	specimen thickness
C	specimen compliance
$[C]$	material's compliance matrix
C_0 – C_4	parameters in geometry function expression
C_m	test rig compliance
C_{ij}	components of the material's compliance matrix
D	dissipated energy rate
$[D]$	Hooke's law matrix
D_{ijkl}	components of Hooke's law matrix
E'	apparent elastic modulus
E_0	equivalent elastic modulus in orthotropic material
E_{AG}	elastic modulus measured against the grain direction
E_i	elastic modulus in orientation i

E_{WG}	elastic modulus measured with the grain direction
F	force
F_c	maximum force
G_i	shear modulus in orientation i
J	J -integral
K	stress intensity factor
K_{Ic}	fracture toughness
K_Q	conditional fracture toughness
R	correlation coefficient
V_l	flight velocity in longitudinal direction (WG)
V_t	flight velocity in transverse direction (AG)
W	specimen width
WG	“with grain” direction
Y	constant in compliance expression
ε_{ij}	strain tensor
ν_{ij}	Poisson's ratio quantifying contraction in direction j as a result of strain applied in direction i
ρ	density
σ_{ij}	stress tensor
ξ	constant in stress intensity factor expression
ζ	constant in stress intensity factor expression

microstructure, which crosses the WG extrusion direction, but the elastic constraint on the crack tip and fracture process zone will differ due to the significant elastic anisotropy of PGA. The TL orientation examines the fracture of the orthogonal plane, which is parallel to the WG extrusion direction.

Some grades of graphite show a linear response to mechanical loading up to the point of fracture [3]. In many other grades of non-irradiated nuclear graphite (e.g. PGA) the stress versus strain characteristic is nonlinear and exhibits both hysteresis and permanent set [4,5]. It cannot be considered a linear elastic material [6,7]. Although not investigated here, it should be noted that when irradiated to a relatively low neutron fluence

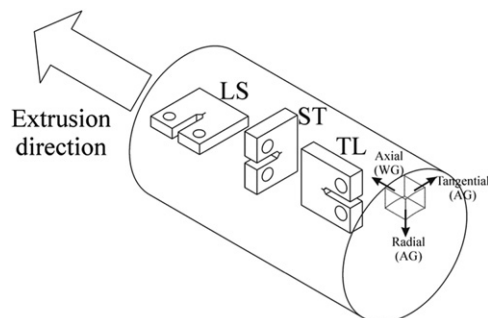
significant irradiation hardening takes place, the stress–strain behaviour becomes linear and both the hysteresis and permanent behaviour are lost [5]. The fracture behaviour of un-irradiated nuclear graphite grades was recently reviewed by Hodgkins et al. [8] who noted the importance of its quasi-brittle characteristic and the role microstructure plays in the deformation of test specimens, the storage of elastic strain energy and their consequent fracture.

This paper aims to measure the effects of orientation on the fracture resistance of PGA graphite. A combined experimental–modelling study has been performed to determine the most appropriate method for the measurement of fracture resistance. It is found that accurate analysis of graphite fracture behaviour from standard-sized test specimens requires an appreciation of microstructural and elastic anisotropy and also the inelastic damage processes that may take place at the crack tip.

Table 1

Typical non-irradiated PGA material properties at ambient temperature (20 °C) [1,51]. Values are given parallel (WG) and perpendicular (AG) to the extrusion direction.

Property	Orientation	
	WG (with grain)	AG (against grain)
Density (g/cm ³)	1.74	
Young's modulus (GPa)	11.7	5.4
Tensile strength (MPa)	17	11
Flexural strength (MPa)	19	19
Compressive strength (MPa)	27	27
Poisson's ratio	0.05	0.12

**Fig. 1.** Different orientations of the extracted specimens.**2. Procedures****2.1. Fracture tests**

A total of 15 compact tension specimens were tested; five in each orthogonal orientation (see Table 3). For each orientation four specimens were tested by monotonic loading at a crosshead displacement rate of 0.2 mm/min and one specimen underwent slow cyclic loading under displacement control at the same rate. The specimen dimensions are given in Fig. 2. The cyclic loading was carried out in order to measure the crack lengths by the

Table 2

Definition of orientations.

Standard orientation	Direction of crack plane normal		Direction of the crack propagation		Direction of the through thickness		The number of tested samples
TL	T	AG	L	WG	S	AG	5
SL	S	AG	L	WG	T	AG	
LT	L	WG	T	AG	S	AG	5
LS	L	WG	S	AG	T	AG	
TS	T	AG	S	AG	L	WG	5
ST	S	AG	T	AG	L	WG	

Table 3
Conditional fracture toughness.

Standard definition	Specimen number	Maximum load (N)		Conditional Fracture toughness (MPa m ^{1/2})	
		F_c	Average	K_Q	Average
LS	1	411	367 ± 36	0.99	0.88 ± 0.08
	2	362		0.87	
	3	316		0.76	
	4	366		0.88	
	5	382		0.92	
ST	1	378	329 ± 41	0.91	0.79 ± 0.10
	2	349		0.84	
	3	312		0.75	
	4	337		0.81	
	5	270		0.65	
TL	1	291	332 ± 68	0.70	0.80 ± 0.17
	2	274		0.66	
	3	411		0.99	
	4	403		0.97	
	5	283		0.68	

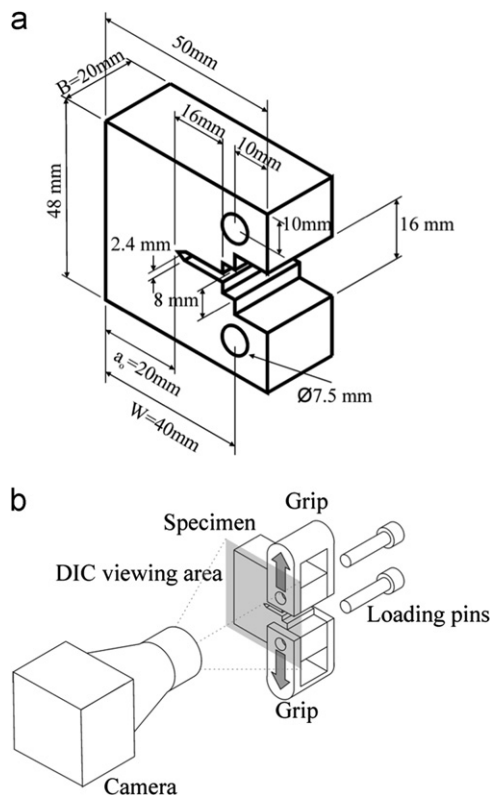


Fig. 2. Fracture test overview: (a) dimensions of compact tension specimen and (b) arrangement of test setup.

compliance (stiffness) method [9], and also to obtain the elastic energy release rate as a function of crack extension [10]. After each cycle, the load was reduced by a crosshead displacement of 0.05 mm, followed by reloading in order to increment the displacement by 0.1 mm. A total of seven cycles were carried out, typically performing two cycles before the maximum load was reached and five cycles thereafter as the crack propagated. The load line displacement was measured using digital image correlation (see Section 2.2), with a precision of 0.8 μ m. The load-cell precision was 0.2% of the reading and the LVDT precision was 0.5% of the reading.

The crosshead displacement, which was directly read from the tensile machine, has contributions from both the load line displacement and the stiffness of the loading chain mechanism, which need to be accounted for to obtain the specimen stiffness. The compound stiffness of the machine, fixtures and loading pins was obtained by subtracting the loading line displacement, obtained using DIC, from the crosshead displacement. We refer to this compound stiffness as the machine stiffness. Using the measured machine stiffness, the load line displacements of those samples for which digital image correlation data were not available were calculated from the crosshead displacement data.

2.2. Digital image correlation (DIC)

Previous investigations [11,12] have shown that digital image correlation is a powerful tool that can be used to detect and characterise cracks in polygranular graphite, using measurements of the full field displacements of the specimen surface. Here, DIC has been used to measure the surface length of cracks via the crack opening displacements, and also to measure the load–line displacements of the specimens. Previous work found that fracture resistance curves in graphite were unreliable when the fracture process zone encountered the boundaries of the specimen [11,13]. It has also been suggested that there is a correlation between the size of the fracture process zone and the inelastic component of the strain energy release rate [14,15]. Observations were therefore made of the inelastic strains (obtained from the surface displacements) associated with the fracture process zone, which is not visible otherwise.

A 4 MPixel 14 bit camera with a 150 mm objective lens was used to monitor the surface of the CT specimens. Images were collected by the LaVision Davis software [16] at the rate of 2 frames/s. Typically 450 and 1100 images were recorded in monotonic and cyclic loading experiments, respectively. These images were analysed by DIC, using multiple interrogations from a window size of 256×256 pixels at an overlap of 50% with two passes, followed by 32×32 pixel windows at an overlap of 75% with three passes. This gave the optimum displacement resolution and spatial mapping of displacements for these experiments. (For further information on the DIC methodology, the reader is referred to [17]).

Cracks can be readily visualised using a strain map, obtained by differentiation of the displacement field, as the crack opening displacement causes artificially high strain levels that are local to the crack path [12]. By defining a sufficient threshold strain value, the crack can be segmented from the strain data and its length is measured. The chosen threshold has a negligible effect on the calculated crack length, due to the steepness of the strain gradients caused by the crack opening [12]. Using the full displacement field, the load line displacement was also obtained from the difference between the average displacement vectors at the two loading pins.

2.3. Measurement of elastic properties

In non-irradiated nuclear graphite, static measurements of the elastic moduli are difficult to obtain due to the short linear elastic region of the stress–strain curve. In addition, it is not generally practical to carry out static modulus measurements on irradiated graphite specimens, which are typically much smaller than standard specimens. Therefore, either ultrasonic or impulse excitation methods may be used to measure nuclear graphite's dynamic elastic properties.

The ultrasonic method is primarily intended for the determination of parameters in isotropic media. In an anisotropic material, such as PGA, the shear modulus determination may be

problematic, due to the interaction between polarised shear waves and the anisotropic properties of the elongated, ‘needle coke’ filler particles. This was neglected in the analysis, however, and a single value of E , G and ν was therefore obtained for each of the WG and AG directions.

Nine samples of graphite cut from the same batch as the fracture samples were examined. The measurements were undertaken on cubes of $40 \times 40 \times 40 \text{ mm}^3$, utilising two orthogonally positioned sets of 1 MHz transducers for longitudinal and transversal excitation. The transducers were operated through an Olympus/Panmetrics 9000 Series Pulser/Receiver. The resultant signal was recorded and analysed on a 200 MHz data capture system. The clamping force in all cases was approximately 50–80 N.

The flight times were measured at the 10% rise point of the first peak, which was chosen to ensure the minimisation of dispersion and scattering effects during the measurement. During the transversal measurements, care was taken to ensure proper alignment of the transducers to maximise the received transversal signal while minimising incidental longitudinal noise. This required good alignment of the transverse plane with the grain direction of the graphite during the against grain (AG) measurement.

The flight velocities (V_l and V_t , respectively in the longitudinal and transverse) measured were used to calculate elastic modulus, shear modulus and Poisson ratio via the following standard equations for the WG and AG directions [18]:

Elastic modulus:

$$E = \rho \left(\frac{3V_l^2 V_t^2 - 4V_t^4}{V_l^2 - V_t^2} \right) \quad (1)$$

Shear modulus:

$$G = \rho V_t^2 \quad (2)$$

Poisson's ratio:

$$\nu = 0.5 \left(\frac{V_l^2 - 2V_t^2}{V_l^2 - V_t^2} \right) \quad (3)$$

2.4. Finite element analysis

The dimensions of the available material precluded the use of compact tension specimens of the standard proportions defined for fracture toughness tests [9]. Finite element simulations of the specimen with dimensions shown in Fig. 2 were carried out using various crack lengths to calculate the compliance and stress intensity factor expressions, and to evaluate their difference from the standard. Nine three-dimensional models (a/W between 0.5 and 0.9 at increments of 0.05) were created using ABAQUS/Standard using 20-node brick elements. Taking account of symmetry, one quarter of each specimen was modelled. Frictionless contact was defined between the rigid loading pin and the specimen. The propagation of the crack was not simulated but rather, a series of models with different original crack lengths were produced. This is an appropriate assumption as long as elastic conditions dominate, and any effects of plasticity in the wake of the crack can be ignored [19,20]. Therefore it was deemed reasonable in a low ductility material such as graphite.

An overview of the finite element mesh is shown in Fig. 3a. The J -integral was calculated using ABAQUS from the contour integral method [21]. Collapsed nodes, or singular elements, were not used in the model, since it has been shown that they do not affect the calculation of J -integral [22] using contour integral methods [23]. Since quadratic elements were used, two different results for the J -integral variation across the crack front were observed. One result is for the values obtained at the element corner nodes and

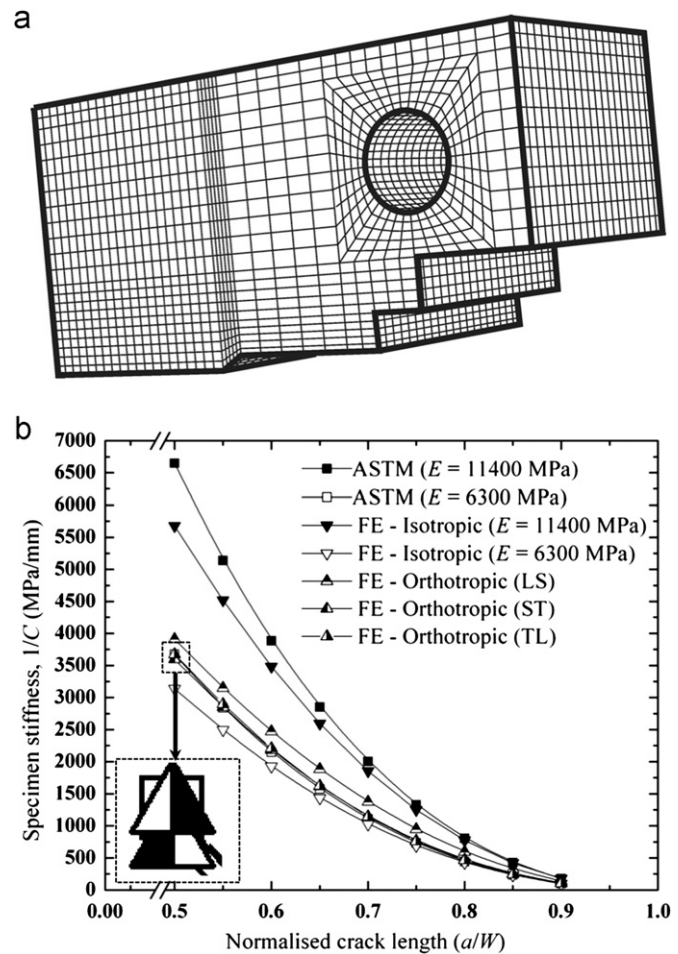


Fig. 3. Finite element study: (a) overview of mesh of a quarter of the specimen and (b) specimen stiffness as a function of normalised crack length with different material properties.

the other for the values at mid-side-nodes. It has been shown that using the corner nodes provide a better representation of J -integral [24], thus this value was selected in this study. The J -integral was found to vary along the crack front across the specimen thickness, with a minimum value at the surface and maximum in the specimen centre. The variation was no more than 13%, however. The form of the variation is consistent with a tendency for crack tunnelling observed in previous studies on graphite [25]. For this reason, the maximum value of the J -integral in the middle of the specimen was taken to be the representative value.

Five sets of simulations with different material properties were performed. Two were isotropic with different properties ($E = 11400 \text{ MPa}$ and $E = 6300 \text{ MPa}$), representative of those measured in the WG and AG directions. Three simulations were with orthotropic properties ($E_{WG} = 11,400 \text{ MPa}$, and $E_{AG} = 6300 \text{ MPa}$) for TL, LS and SL specimen orientations (see Fig. 1). Details of the anisotropy implementation in the finite element model are given in appendix A.

2.5. Fracture parameters

Using the finite element simulation described in the previous section, the compliance C and geometry functions $f(a/W)$ were extracted and are presented in Eqs. (4)–(9), for comparison with

experimental data, and hence to obtain resistance curves of the energy release rate as a function of crack growth.

Two types of resistance curves can be thus obtained by these different techniques for each specimen: (i) direct experimental and (ii) numerical. In the direct experimental technique, the crack length is measured using digital image correlation (see Section 2.2) and the energy release rate is obtained from the cyclic load–load line displacement curve using Turner and Kolednik's method. In the numerical technique, the crack length is obtained from the unloading compliance expressions in Eq. (5), and the energy release rate is calculated using geometry factors and Eq. (9). Within the numerical technique, three different cases can be considered for the compliance and geometry factors: (i) the values suggested by standards such as ASTM E399 can be used which are calculated by boundary collocation analysis, or three-dimensional finite element analysis can be used to find a new set of calibrating parameters with the assumption of (ii) isotropic or (iii) orthotropic material behaviour.

3. Results

3.1. Elastic modulus measurements

The results of the dynamic Young's modulus and Poisson's ratio measurements are reported in Table 6. The discrepancies compared with the typical literature values for Young's moduli listed in Table 1 are moderate ($<17\%$), and may be due to manufacturing batch variations and also the inherent issues of carrying out, and defining, the static Young's modulus for a nonlinear material such as non-irradiated Graphite. The measured values for Young's modulus were used in the finite element modelling, giving a ratio of E_{AG}/E_{WG} of 0.55 (compared to $E_{AG}/E_{WG}=0.46$ for the values in Table 1).

The differences in Poisson's ratio are attributed to the necessary assumption of isotropic behaviour in Eqs. (1)–(3), so the calculated values are not regarded necessarily as accurate. However, the effect of Poisson's ratio in this range on the specimen compliance is not large, and is not significant in comparison to the effects of the anisotropy of Young's modulus. The values in Table 6 were therefore used in the finite element simulations, as described in appendix A.

3.2. Fracture

3.2.1. Fracture toughness

Examples of the typical data for load–load line displacements curves for the three orientations are shown in Fig. 5. The effect of orientation on specimen stiffness is clear, as is significant scatter in the fracture load. The TL specimens loaded in the WG direction are stiffer than those loaded in the AG direction (LS and ST). The relative horizontal displacement of the loading pins, measured via DIC, never exceeded 0.02 mm, which is less than 5% of the typical crack opening displacement upon fracture initiation. That is, the

Table 6
Measured elastic properties.

Property	Direction	
	WG	AG
Young's modulus (GPa)	11.4 ± 0.2	6.3 ± 0.2
Shear modulus (GPa)	4.4 ± 0.2	2.8 ± 0.2
Poisson's ratio	0.29 ± 0.02	0.13 ± 0.02

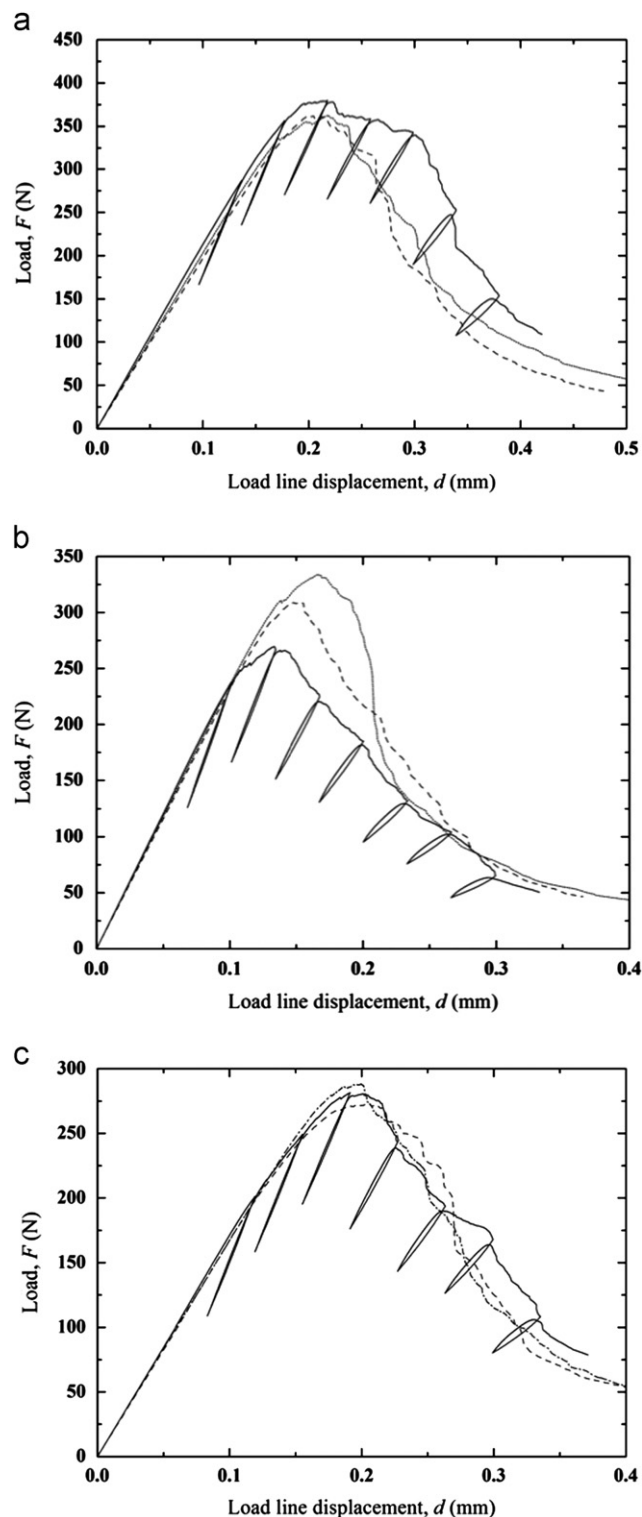


Fig. 5. Examples of load–load line displacement response of tested specimens in (a) TL, maximum load varies between 411 N and 356 N, (b) LS, maximum load varies between 403 N and 270 N and (c) ST, maximum load varies between 378 N and 283 N. The load line displacement was measured using DIC for samples experiencing unloading and calculated from the head displacement and machine stiffness for the rest.

measured displacement vector deviates about 3° from the pure opening direction. This causes a slight degree of shear (mode II) loading, which is discussed later on.

Using the procedures recommended by the standards (e.g. ASTM E399 [2]), the provisional fracture toughness K_Q was calculated from the load–load line displacement curves (Table 3). However, according to the ASTM recommendations, none of these provide valid fracture toughness values (i.e. K_{Ic}), due to the significant nonlinearity in the load–load line displacement, which is due to stable crack growth.

3.2.2. Crack lengths

Comparing the measured and modelled stiffness of uncracked specimens provides information on the validity of the finite element model and the defined material properties. In each cyclic test, at least two loading cycles were completed before crack propagation occurred (e.g. cycles 0 and 1 in Fig. 4). The stiffness values measured in the initial loading (marked cycle 0 in Fig. 4) are not necessarily reliable as they may include displacements from specimen settling at the loading pins, although in fact the stiffness calculated from the loading stage of cycle 0 was found to be less than 3% different from that from the loading stage of cycle 1. The stiffness of the specimens during unloading in cycle 0 and loading in cycle 1 was calculated over the mid-range of load (between 45% and 67% for TL, 41% and 72% for LS, and 46% and 82% for ST of their respective maximum load), where linear behaviour was clearly observed. The specimen stiffness data for the cycle 1 loading (Fig. 4) are reported in Table 7 together with the values obtained from the standard ASTM expression (Eq. (5), which assumes isotropic elastic properties) and the isotropic and orthotropic finite element simulations. Some significant differences are observed. The measured stiffness values are comparable in all cases to the modelled isotropic stiffness obtained using the lower AG modulus (for either the ASTM and FE models), irrespective of the sample orientation. This shows that the lower modulus dominates the specimen deflection under load. The orthotropic finite element model is more accurate and provides a specimen stiffness that is within 17% of the measured stiffness for all three orientations, correctly predicting their relative values also. In the absence of a complete orthotropic model, however, the compliance of the specimen in anisotropic PGA may therefore be calculated approximately using a lower value of elastic modulus.

As shown in previous investigations [12], cracks can be visualised by DIC analysis using the strain fields; this is because the crack opening displacement causes artificially high strain levels local to the crack. By defining a suitable opening strain threshold value, the crack can be visualised. It has been shown that the threshold has little effect on the calculated crack length [12], due to the steepness of the strain gradient. The opening strain threshold was selected in this study to be 1%, which was

applied to a map of the maximum principal strain. Observation of fracture process zone was achieved by detecting the microcracks that formed around the crack tip, which have smaller crack opening displacements. This may be done by reducing the opening strain threshold, for instance, to 0.5%.

The crack length was measured as the linear dimension of the dominant crack, as indicated in Fig. 6. An example of the opening strain distribution, obtained by DIC, is shown in Fig. 7, measured for a path passing along the length of the crack. The figure confirms that the strain due to the crack opening is sufficiently large for the crack dimensions to be insensitive to the arbitrary strain threshold of 1%. The main crack is surrounded by an array of microcracks, located predominantly towards the crack tip. Crack branching and bridging were also observed, but for the limited number of specimens no clear trends were observed in the characteristics of crack bridging and branching for the different orientations. The surface crack bridging, observed in some cases (e.g. Fig. 6b), was ignored in the crack length measurements. The dimension of fracture process zone, which has a size of the order of 2–5 mm, is shown in Fig. 7 to be obtained approximately using a 0.5% opening strain threshold.

The crack lengths derived from the measured specimen stiffness (i.e. inverse of compliance calculated by Eq. (5) using appropriate coefficients from Table 5 for the ASTM recommendation and the linear elastic FE simulations for isotropic and orthotropic materials) are reported in Table 8, together with the surface length observed by DIC. The ASTM and isotropic FE solution values are similar (within 11%) since the specimen geometry deviates only a little from the standard design (differences in the treatment of the load application in the FE model become less significant as the specimen stiffness decreases). The data for the increase in crack length from the notch, calculated from three different numerical methods, namely ASTM, FE isotropic and FE orthotropic are shown in Fig. 8 as a function of the equivalent surface crack extension measured using the digital image correlation method. The crack extensions calculated using the orthotropic FE model are generally closer to the values measured by DIC, particularly for the TL direction (Fig. 8a). However, the percentage differences between *total* crack lengths, obtained using DIC and the various finite element methods are generally less than 10%; these are reported in Table 8.

3.2.3. Fracture resistance curves

The conditional fracture toughness values were considered not to be valid due to the nonlinearity caused by stable crack growth. Therefore fracture resistance curves were measured. The fracture resistance curves obtained for the three orientations by different

Table 7

Stiffness of the non-cracked specimens in three orientations from different methods. The difference between the experimental stiffness and model stiffness is shown (%Err).

	Experiment			ASTM		Isotropic FE		Orthotropic FE	
	No.	Load range (N)	1/C	1/C (N/mm)	%Err	1/C (N/mm)	%Err	1/C (N/mm)	%Err
LS	1U	171–253	3550	6645 ^a	87.2	5679 ^a	60.0	3912	10.2
	2L		3433	3674 ^b	4.86	3138 ^b	11.6		
ST	1U	111–196	3218	6645 ^a	93.6	5679 ^a	65.4	3672	14.1
	2L		3229	3674 ^b	7.0	3138 ^b	8.6		
TL	1U	1230–232	2983	3674 ^b	14.2	3138 ^b	2.5	3596	14.7
	2L		2957		13.8		2.8		
	1U				23.2		5.2		20.5
	2L				24.3		6.1		

No.: cycle number, C: compliance, L: loading, U: unloading; i.e. 2L is second loading cycle

^a $E=11400$ MPa.

^b $E=6300$ MPa.

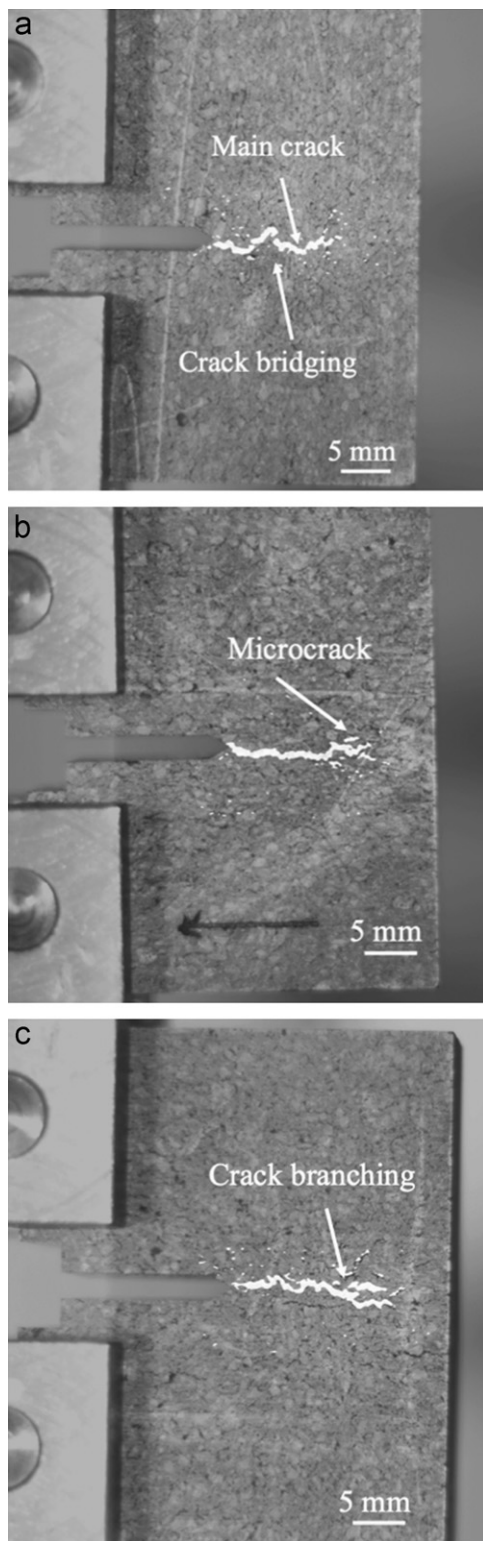


Fig. 6. Examples of digital image correlation analysis showing the propagating crack and microcracking in the fracture process zone around the main crack in different orientations: (The figures show the data obtained at the maximum load at the last loading cycle). (a) LS—crack bridging is visible, (b) ST—microcrack formation around the main crack tip is visible and (c) TL—crack branching is visible.

analysis methods are shown in Fig. 9. In each case of the numerical method the crack lengths were obtained by the stiffness method and the stress intensity factors were calculated from Eqs. (7)–(9) using the relevant FE analysis. The small difference of

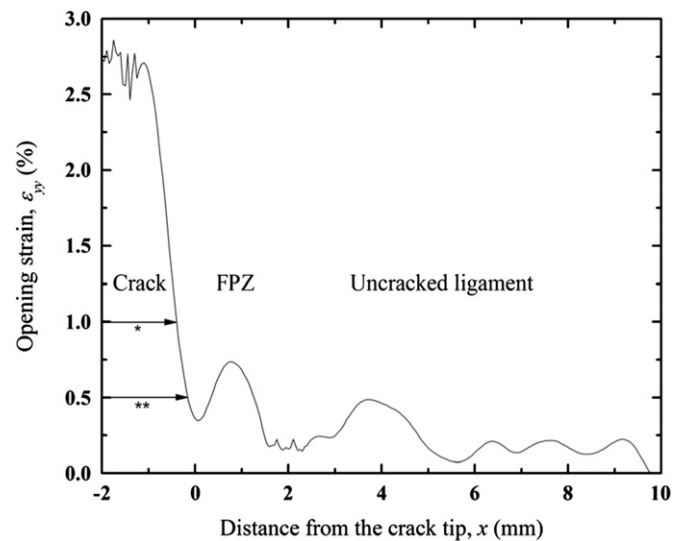


Fig. 7. Example of opening strain distribution along a path passing through the crack for a specimen in SL, *: location of the crack tip used in crack length calculations considering 1% opening strain threshold, **: location of the crack tip used in crack length calculations considering 0.5% opening strain threshold.

Table 8

Crack lengths calculated or measured from different methods.

Cycle	Direct	Numerical								
		DIC <i>a</i> (mm)	ASTM		Isotropic FE				Orthotropic FE	
			<i>a</i> (mm)	Err (%)	<i>a</i> ^a (mm)	Err (%)	<i>a</i> ^b (mm)	Err (%)	<i>a</i> (mm)	Err (%)
LS	3	23.5	25.8	9.8	25.2	7.2	20.6	−12.3	22.6	−3.8
	4	24.5	27.4	11.8	27.0	10.2	22.9	−6.5	24.8	1.2
	5	26.4	28.5	7.9	28.2	6.8	24.4	−7.6	26.3	−0.4
	6	29.1	29.5	1.4	29.3	0.7	25.9	−11.0	27.7	−4.8
	7	31.5	30.9	−1.9	30.7	−2.5	27.9	−11.4	29.5	−6.3
ST	3	22.5	22.6	0.4	−	−	22.8	1.3	21.6	−4.0
	4	24.0	24.2	0.8	−	−	24.4	1.7	23.5	−2.1
	5	27.7	26.6	−4.0	−	−	26.8	−3.2	26.0	−6.1
	6	29.9	28.6	−4.3	−	−	28.8	−3.7	28.3	−5.4
	7	30.5	29.8	−2.3	−	−	29.9	−2.0	29.5	−3.3
TL	3	22.2	21.7	−2.2	−	−	21.6	−2.7	21.7	−2.3
	4	27.0	23.3	−13.7	−	−	22.5	−16.7	23.4	−13.3
	5	29.1	26.1	−10.3	−	−	25.5	−12.4	26.3	−9.6
	6	29.7	28.1	−5.4	−	−	27.7	−6.7	28.3	−4.7
	7	31.0	30.4	−1.9	−	−	30.1	−2.9	30.6	−1.3

^a $E = 11400$ MPa.

^b $E = 6300$ MPa.

the order of 10% in the calculated and measured total crack lengths has a smaller effect on the stress intensity factor (less than 2% for crack lengths with $a/W < 0.8$). The calculated stress intensity factors were converted to equivalent J -integral using Eqs. (7) and (8).

In the case of the direct method, the surface crack length was measured using digital image correlation analysis, since this gave a better measure of the crack growth increments than estimation from the compliance. The elastic energy release rate associated with this increment was calculated from the area under the load–load line displacement curve, as recommended by Turner and Kolednik [29]. It was considered appropriate to address only the elastic component of the energy release rate, as it has been shown that this contributes around 75% of the total energy release rate

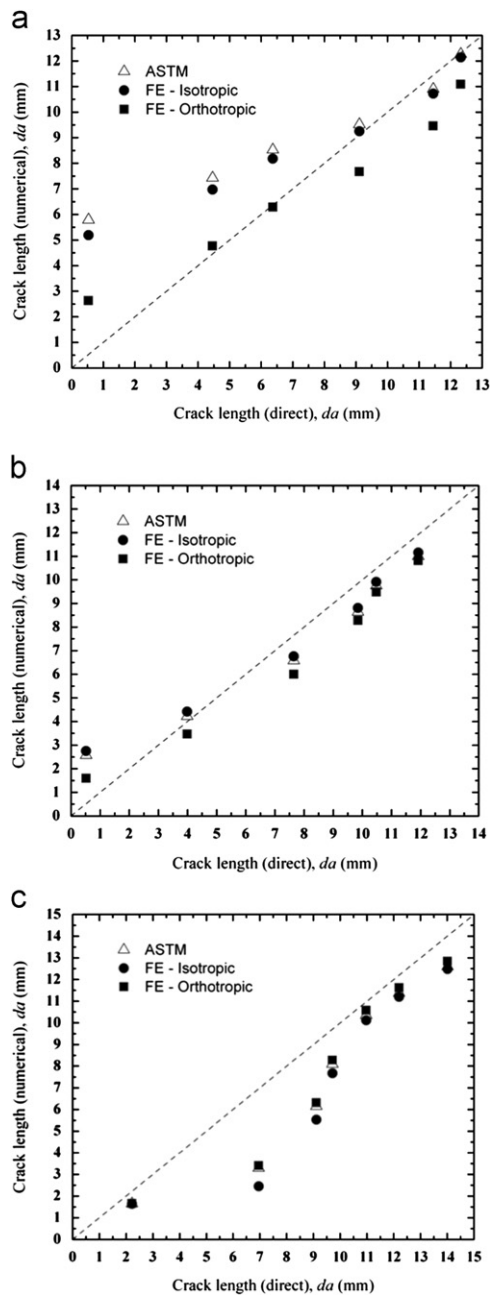


Fig. 8. Crack length increase calculated from different methods: (a) LS, (b) ST and (c) TL. One to one line is shown in dashed.

[11] in this grade of polygranular graphite. This assumption may not be appropriate for other grades of graphite [13,32].

In all cases, the fracture resistance curve (Fig. 9) starts with a rising trend and attains a maximum followed by a steep reduction as the crack propagates. Similar trends have been reported by other researchers for isotropic and anisotropic nuclear grade graphite (e.g. [13,33]). Fig. 9 also shows that there is a little difference (less than 5%) between the J - R curves measured by the numerical method using the standard expressions and the isotropic finite element simulations. This is to be expected, since the differences in predicted stiffness are minor. The orthotropic FE model was shown earlier to more accurately simulate the specimen stiffness than isotropic models, and the numerical method J - R curves obtained from the orthotropic finite element analysis differ from the isotropic solutions by up to 20% in the TL

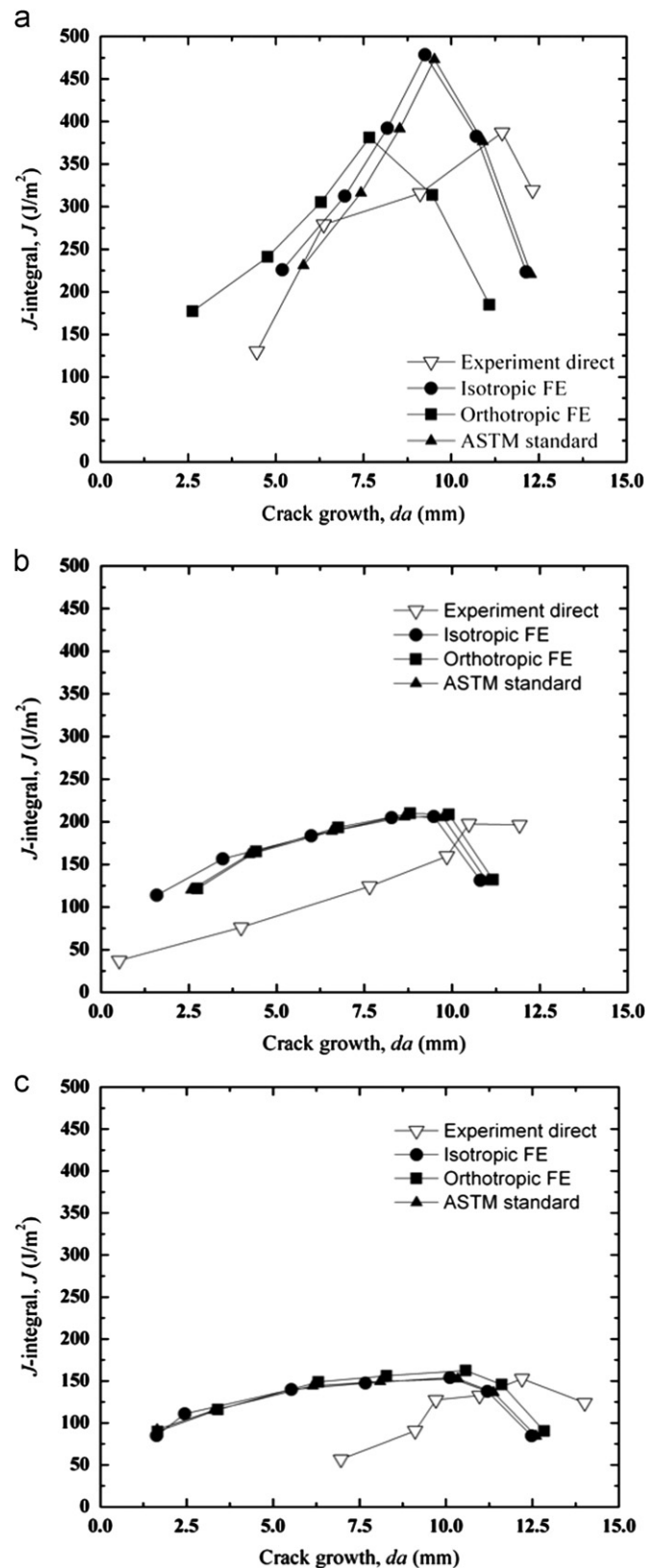


Fig. 9. Fracture resistance (J - R) curves measured directly from load–load displacement curves (direct method) and calculated from isotropic finite element model and orthotropic finite element models (numerical method) in (a) LS, (b) ST and (c) TL.

orientation (i.e. crack propagating in the WG direction). For this orientation, the orthotropic FE model calculates a higher J - R curve compared with the isotropic FE model up to the peak in

Table 9

Energy per unit area and energy rates released due to crack propagation measured from different methods (all values are in J/m²).

	Cycle	Direct		Numerical		
		Elastic ^a	Plastic ^b	ASTM	Isotropic FE	Orthotropic FE
LS	3	130.01	108.91	230.95	225.74	177.16
	4	279.20	258.77	316.24	312.53	240.90
	5	315.78	276.79	391.59	392.13	305.25
	6	387.24	455.19	473.00	478.37	381.19
	7	319.40	646.58	376.58	382.64	313.70
ST	3	37.25	109.73	121.66	120.23	113.84
	4	76.04	118.47	165.16	161.56	156.56
	5	124.34	209.88	193.26	188.93	183.61
	6	159.51	246.40	209.77	205.80	204.77
	7	197.52	867.42	208.50	204.94	206.22
TL	3	56.70	320.10	91.99	84.78	89.70
	4	90.64	230.81	115.11	110.85	115.86
	5	127.39	318.40	144.17	139.77	148.76
	6	132.58	734.54	149.33	147.52	156.17
	7	152.68	1158.70	152.68	154.12	162.38

^a Calculated by using elastic part of energy measured as recommended by Turner and Kolednik [29].

^b Calculated by using the energy dissipation rate measured as recommended by Sumpter [41].

the *J*–*R* curve. After the peak, the trend reverses and a lower *J*–*R* curve is calculated from orthotropic FE model compared with the isotropic FE model. In LS and ST orientations (i.e. crack propagating in the AG direction, loaded in either WG or AG direction), the difference between the isotropic and orthotropic solutions does not exceed 5%.

The direct *J*–*R* curves (i.e. crack extension from DIC and energy release rate calculated from the Turner and Kolednik [29] method) differ significantly from the ASTM or finite element analyses, by up to 150% at some points. The same scales have been used in Fig. 9a–c for easier comparison of the effect of orientation on the *J*–*R* curves. The values are reported in Table 9.

Nonetheless, regardless of the method used to measure the fracture resistance, the LS orientation (i.e. crack loaded parallel to the WG direction and propagating in the AG direction) demonstrates a higher resistance to crack propagation than TL and ST orientations (i.e. crack propagating in either the WG or AG direction, along a plane with its normal perpendicular to the WG direction).

4. Discussion

This study has investigated the effects of the material anisotropy in the fracture resistance curves of PGA nuclear graphite, for crack propagation with (WG) and against (AG) the extrusion direction. Although the measured and simulated stiffness of the specimens do not agree unless an orthotropic material model is considered, the differences observed between the *J*–*R* curves calculated from isotropic or orthotropic material models by the numerical method are generally less than 20%. For instance, for a standard specimen with *a*/*W*=0.5, the stiffness calculated from the orthotropic analysis can be almost double that of the equivalent isotropic analysis (see Table 7). The relatively small effect on the numerical *J*–*R* curves is also due to the difference in isotropic and orthotropic stiffnesses, which is used to calculate crack length, reducing when longer cracks are considered.

The observed differences between the resistance curves in different orientations are significantly larger than the expected

experimental errors. For instance, the uncertainty in the crack lengths obtained from stiffness measurements can be estimated from the uncertainty in a linear fit to the unloading load–load line displacement data. First order regression was used to measure the stiffness. In all cases the uncertainty was less than 2% (correlation coefficient $R^2 > 0.98$). The corresponding uncertainty in the calculated stress intensity factor is 0.25% of the measurement reading value, due to the sensitivity of the load cell used. It is quite insensitive to error in the crack length in the range considered, which is the designed intent of compact tension specimens. The potential error from misalignments can be estimated from the relative horizontal displacement of the loading pins, which was measured by digital image correlation to never exceed 0.02 mm. This is less than 5% of the typical crack mouth opening displacement upon fracture. Assuming a linear relationship between energy release rate and crack tip displacement [34], a 5% shear displacement in the total opening displacement will cause less than 5% error in the calculated mode I energy release rate.

The fracture resistance curves, regardless of the method by which they were obtained, start with a rising trend, reach a maximum followed by a steep reduction as the crack grows further. The reduction has been suggested to be the result of the fracture process zone approaching the physical boundaries of the specimen [13,33]. The observation of the fracture process zone by digital image correlation (Fig. 6) corroborates this suggestion. The reduction in the fracture resistance curves coincides with crack growth of roughly 10 mm in these experiments (see Fig. 9). There is no noticeable trend between the distance at which this occurs and the elastic modulus in the crack propagation direction, implying that this is not an elastic interaction. The reduction occurs when the fracture process zone (of the order of 5 mm—see Fig. 6) is approximately 5 mm from the back face of the specimens, which is consistent with the effect being dominated by the development of the fracture process zone in the un-fractured specimen ligament.

There are quite significant differences between the *J*–*R* curves calculated by the numerical and the direct methods. The direct method yields lower values for smaller crack lengths and higher values for long cracks. This is due to intrinsic differences in the calculation methods, and not due to differences in the crack length obtained by direct observation or from compliance (using the direct measurement of crack length in the numerical method changes the *R*-curve by less than 12%, which is due to the relative insensitivity of the CT specimen stiffness to crack length). The *J*-integral obtained by the FE numerical method is equivalent to the instantaneous energy release rate obtained by the domain integral method [35] (assuming elastic behaviour), which is essentially calculated by considering the strain energy change for a virtual crack extension. The Turner and Kolednik method, employed in the direct method, calculates the average elastic strain energy released for a measurable increment in crack length (for more details see [36–39]), which is referred to as normalised strain energy, hereafter, for simplicity. If the second derivative of strain energy release with respect to crack length is non-zero, the averaged value obtained by the direct method over significant increments of crack length may overestimate, or underestimate, the true strain energy release rate. Convergence between the two methods would be obtained only if the normalised energy release is calculated for sufficiently small crack growth increments (see for example [40]), or if the *R*-curve is independent of crack length (i.e. a plateau) where the second derivative of strain energy release with respect to crack length is close to zero. This may be observed in Fig. 9. The *J*–*R* curves measured in this study by the numerical method, which are similar to previous investigations (e.g. [13,33]), show an initially steep and nonlinear trend with crack growth. This is where the greatest difference from the direct

experiment (Turner and Kolednik) J – R curve is observed. In the vicinity of the numerical method J – R plateau the numerical and the direct methods yield similar values (around 3% difference at $da \approx 10$ mm—see Fig. 9). Significant differences (generally more than 45%) are again observed when the numerical method J – R curve falls after the plateau where the inelastic fracture process zone meets the physical boundary of the specimen. The direct-experimental method should therefore only be applied in cases where sufficiently short crack growth increments can be studied. The numerical method, using an orthotropic material model, is preferred for an anisotropic nuclear graphite such as PGA.

To ensure that the inelastic part of the dissipated energy does not dominate the fracture behaviour of PGA (i.e. the mechanism is indeed fracture and not tearing), the dissipated energy rate (D) was calculated from the load–load line displacement graphs for specimens that underwent cyclic loading, following Sumpter [41]. The values are reported in Table 9, in which it can be seen that neither the elastic nor plastic energy release rates correspond to the energy release rates obtained from the finite element simulations. The inelastic share of energy release rate on PGA is sufficiently substantial to cause deviation from pure elastic brittle behaviour, though its contribution is not at the level to dominate the fracture behaviour and change the mechanism to tearing. The effects of constraint change (i.e. change in the size of fracture process zone [14]) on the relative contributions of released elastic and dissipated plastic energies as the crack propagates means that a more thorough investigation on the inelastic behaviour of graphite would be required to establish a two-parameter fracture mechanics description (e.g. J – T [42] within its limits), which could account for both released elastic and dissipated inelastic energies. That, however, is beyond the scope of this work.

Since the inelastic region in front of the crack tip is small compared with the size of the specimen, a small scale yielding approach can be used. An effective crack length can therefore be defined which is comprised of the physical macromechanical crack and the radius of fracture process zone. Accurate measurement of the fracture process zone requires more sophisticated observations, which are beyond the objectives of this paper. A first approximation, however, may be obtained by using Irwin's equation for the crack tip plastic zone; considering the ultimate tensile strength for PGA as the yield stress, this predicts a fracture process zone of the order of 1.7 mm in the SL, 1.0 mm in the ST and 0.8 mm in the TL orientations. These calculated fracture process zones are generally smaller, but of similar order, than observed by digital image correlation (e.g. Fig. 7 shows a zone of approximately 1–2 mm in the SL orientation), as the mechanical softening of graphite in the fracture process zone is neglected in the approximation. Nonetheless, such a correction to the effective crack length causes less than 14% variation in the calculated stress intensity factor.

An alternative to the energy-based approach discussed in this paper is the use of the crack tip opening displacement (CTOD) or crack tip opening angle (CTOA) as fracture criteria. For instance, researchers have successfully used a critical CTOA criterion to estimate toughness of metallic components, especially in the case of mixed mode fracture (e.g. [34]). However, its measurement is not straightforward, thus it is not widely used in fracture assessment procedures by engineers. In particular it is difficult to locate the tip of the crack and to measure crack opening behaviour in porous, brittle, materials such as graphite.

The observation of resistance curves shows that PGA, a virgin non-irradiated, nuclear graphite, cannot be considered a linear elastic material with a single value of fracture toughness. This corroborates earlier findings that nuclear graphite shows some degrees of inelastic behaviour [11,43]. Such a behaviour can be simulated best with a model capable of showing softening before

final failure, and a Hillerborg et al. [44] type cohesive zone model might be used for this purpose. Such cohesive models require the shape of the traction-separation law, cohesive energy, maximum stress and critical displacement at which the softening behaviour starts, though it has been shown that the shape of the traction-separation law has little effect on the crack initiation load, specially when the cohesive energy is low and constant [45–47]; this would be appropriate for graphite. Comprehensive studies by Cornet et al. [48] and later Schwalbe et al. [49] have shown that for quasi-brittle materials such as graphite, the cohesive energy can be considered equal to the energy release rate measured from a standard high constraint fracture test and the maximum stress in the cohesive model can be considered to be equal to the tensile strength. By employing these assumptions, a bridge could be constructed between the energy approach presented here and the cohesive model. However, it should be mentioned that the geometry and loading condition dependency of cohesive zone model parameters has been challenged [50].

The nonlinear and anisotropic behaviour of PGA is thus apparent in several ways: (1) anisotropy of material properties, shown in the form of the three different elastic moduli and Poisson's ratios; (2) a short region of nonlinear, inelastic behaviour of mechanical properties which is observed at the end of linear mechanical behaviour region; this is judged to be negligible in this study; (3) the anisotropic fracture initiation behaviour, which is discussed in the form of K_Q in three different orientations and (4) the anisotropic stable crack propagation behaviour which is discussed in the form of J – R curves in the different orientations.

The stiffness measurements and orthotropic finite element modelling show that the lower of the two anisotropic moduli dominates the specimen stiffness and hence the stored elastic energy. Higher fracture resistance during stable crack growth is measured for the LS orientation, i.e. when the crack propagation plane is perpendicular to the stiffer extrusion direction (WG), compared with the cases where the crack propagation plane is parallel to the extrusion direction (ST and TL). The fracture resistance is not observed to depend on the direction of fracture within the WG plane; the difference (15%) observed between these two conditions (i.e. ST vs. TL) using the orthotropic numerical method is not very significant. It might be influenced by the difference in the elastic modulus normal to the crack plane or be due to material variability.

This is consistent with the general view [11] that for anisotropic nuclear graphite microstructures, where the needle coke filler particles are aligned in the extrusion direction, the toughness in the LS orientation (i.e. crack propagation direction in the AG direction) is increased; the crack follows the easier, but more tortuous, path around filler particle rather than through them. For a crack propagating in the WG direction, the easier fracture path cleaves the needle coke filler particles, developing a lower resistance to fracture.

5. Conclusions

- The stiffness of PGA nuclear graphite, when measured with the grain direction is twice its similar parameter when measured against the grain.
- The fracture resistance is most accurately obtained using finite element solutions for the instantaneous strain energy release rate that include the anisotropy of the elastic properties.
- The crack length can only be accurately derived by the cyclic unloading technique if the stiffness of a model with orthotropic material properties is considered. However, the effect of any errors in crack length and the corresponding fracture

resistance due to a neglect of anisotropy are not large (i.e. < 12%) for a compact tension specimen.

- The highest mode I fracture resistance is measured in virgin PGA graphite for the LS orientation (i.e. crack propagation in a plane that is perpendicular to the stiffer WG extrusion direction); it is 47% greater than orientations that contain the extrusion direction (i.e. ST and TL, where the crack propagation plane is perpendicular to the AG direction). This is consistent with the trends in other anisotropic nuclear graphites.

Acknowledgments

Authors would like to thank R. Summers for preparing the samples and performing the fracture tests and R. Gater for the undertaking of the ultrasonic tests. P.M. Mummery (University of Manchester) and M.R. Goldthorpe (Martin Goldthorpe Associates: Engineering Analysis) are gratefully acknowledged for their valuable discussions. B.J. Marsden and M.J.J. Schmidt acknowledge the support of Health and Safety Executive (Office of Nuclear Regulation). T.J. Marrow and M. Mostafavi acknowledge the support of the Oxford Martin School.

Appendix—anisotropy

To study the effects of orthotropy on energy release rate and stiffness of the specimens, four different material properties were considered: conventional isotropic material and an orthotropic material with crack propagating in three orientations. The stiffness matrix D , defining the relationship between stress tensor σ and strain tensor ε for an orthotropic material can be written as

$$\sigma_{ij} = [D]\varepsilon_{ij} \quad (10)$$

$$[D] = \begin{bmatrix} D_{1111} & D_{1122} & D_{1133} & 0 & 0 & 0 \\ & D_{2222} & D_{2323} & 0 & 0 & 0 \\ & & D_{3333} & 0 & 0 & 0 \\ & & & D_{1212} & 0 & 0 \\ & SYM & & & D_{1313} & 0 \\ & & & & & D_{2323} \end{bmatrix} \quad (11)$$

where

$$D_{1111} = E_1(1 - \nu_{23}\nu_{32}) \quad (12)$$

$$D_{2222} = E_2(1 - \nu_{13}\nu_{31}) \quad (13)$$

$$D_{3333} = E_3(1 - \nu_{12}\nu_{21}) \quad (14)$$

$$D_{1122} = E_1(\nu_{21} + \nu_{31}\nu_{23})\gamma = E_2(\nu_{12} + \nu_{32}\nu_{13})\gamma \quad (15)$$

$$D_{1133} = E_3(\nu_{13} + \nu_{12}\nu_{23})\gamma = E_1(\nu_{31} + \nu_{21}\nu_{32}) \quad (16)$$

$$D_{2233} = E_2(\nu_{32} + \nu_{12}\nu_{31})\gamma = E_3(\nu_{23} + \nu_{21}\nu_{13})\gamma \quad (17)$$

$$D_{1212} = G_1 \quad (18)$$

$$D_{1313} = G_2 \quad (19)$$

$$D_{2323} = G_3 \quad (20)$$

$$\gamma = \frac{1}{1 - \nu_{12}\nu_{21} - \nu_{23}\nu_{32} - \nu_{31}\nu_{13} - 2\nu_{21}\nu_{32}\nu_{13}} \quad (21)$$

where E_i and G_i are elastic and shear moduli in direction i and ν_{ij} is the Poisson ratio quantifying contraction in direction j due to applied force in direction i . Since the equations are normalised with respect to the elastic modulus, the absolute values of the elastic moduli in three orientations are not important and only

Table A1

Orthotropic Hooke's law parameters.

Tensile parameters (GPa)	D_{1111}	12.761
	D_{2222}	6.84
	D_{3333}	6.84
	D_{1122}	2.35
	D_{1133}	2.35
	D_{2233}	1.26
Shear parameters (GPa)	D_{1212}	2.8
	D_{1313}	2.8
	D_{2323}	4.8
Poisson's ratios	ν_{12}	0.29
	ν_{23}	0.13
	ν_{31}	0.16

the ratios between them matter. The ratio $E_3/E_1 = E_2/E_1 = 0.55$ was used, as measured experimentally. The experimental measurements obtain ν_{12} and ν_{23} whereas $\nu_{21} = \nu_{31}$ can be estimated from $\nu_{31}/E_3 = \nu_{13}/E_1 = \nu_{32}/E_2$ to satisfy Eqs. (15)–(17). In the isotropic case ($E_1 = E_3$), then $D_{2222} = D_{3333}$, $D_{1122} = D_{1133}$, $D_{1212} = D_{1313}$ and also $\nu_{12} = \nu_{13}$, $\nu_{23} = \nu_{32}$. Similarly the compliance matrix C can be written as

$$\varepsilon_{ij} = [C]\sigma_{ij} \quad (22)$$

$$[C] = \begin{bmatrix} C_{11} & C_{12} & C_{13} & 0 & 0 & 0 \\ C_{21} & C_{22} & C_{23} & 0 & 0 & 0 \\ C_{31} & C_{32} & C_{33} & 0 & 0 & 0 \\ 0 & 0 & 0 & C_{44} & 0 & 0 \\ 0 & 0 & 0 & 0 & C_{55} & 0 \\ 0 & 0 & 0 & 0 & 0 & C_{66} \end{bmatrix} \quad (23)$$

where

$$C_{11} = 1/E_1 \quad (24)$$

$$C_{12} = -\nu_{21}/E_2 \quad (25)$$

$$C_{13} = -\nu_{31}/E_1 \quad (26)$$

$$C_{21} = -\nu_{12}/E_1 \quad (27)$$

$$C_{22} = 1/E_2 \quad (28)$$

$$C_{23} = -\nu_{32}/E_3 \quad (29)$$

$$C_{31} = -\nu_{13}/E_1 \quad (30)$$

$$C_{32} = -\nu_{23}/E_2 \quad (31)$$

$$C_{33} = 1/E_3 \quad (32)$$

$$C_{44} = 1/G_{12} \quad (33)$$

$$C_{55} = 1/G_{13} \quad (34)$$

$$C_{66} = 1/G_{23} \quad (35)$$

In the transversely isotropic case, E_1 is the WG direction, E_2 and E_3 are the AG directions; values are reported in Table A1.

References

- [1] A.N. Jones, L. McDermott, B.J. Marsden, T.J. Marrow, Review of the Characterization of Nuclear Graphites in UK Reactors Scheduled for Decommissioning, IAEA, 2010.
- [2] ASTM-E399, Standard Method for Plane-Strain Fracture Toughness of Metallic Materials, E399, ASTM, 2004.

- [3] S.S. Zhunisbekov, V.P. Naumenko, G.S. Volkov, G.S. Pastukhov, *Strength Mater. Engl. Tr.* 15 (1983) 1703–1708.
- [4] H.H.W. Losty, J.S. Orchard, in: S. Mrozowaki, M.L. Studebaker, P.L. Walker (Eds.), *Fifth Conference on Carbon*, MacMillan, Pennsylvania State University, 1962.
- [5] R. Taylor, R.G. Brown, K. Gilehrst, E. Hall, A.T. Hodds, B.T. Kelly, F. Morris, *Carbon* 5 (1967) 519–531.
- [6] P.J. Heard, M.R. Wootton, R. Moskvic, P.E.J. Flewitt, *J. Nucl. Mater.* 418 (2011) 223–232.
- [7] E. Schlagen, P.E.J. Flewitt, G. Smith, A. Crocker, A.D. Hodgkins, *Key Eng. Mater.* 452–453 (2011) 729–732.
- [8] A.D. Hodgkin, T.J. Marrow, M.R. Wootton, R. Moskvic, P.E.J. Flewitt, *Mater. Sci. Technol.* 26 (2010) 899–907.
- [9] ASTM-E1820, *Standard Method for Measurement of Fracture Toughness*, E1820, ASTM, 2001.
- [10] J.A. Begley, J.D. Landes, *National Symposium on Fracture Mechanics Part II: Fracture Toughness*, ASTM, Philadelphia, 1971, pp. 1–23.
- [11] T.H. Becker, T.J. Marrow, R.B. Tait, *J. Nucl. Mater.* 414 (2011) 32–43.
- [12] M. Mostafavi, T.J. Marrow, *Eng. Fract. Mech.* 78 (2011) 1756–1770.
- [13] P. Ouagne, G.B. Neighbour, B. McEnaney, *J. Phys. D: Appl. Phys.* 35 (2002) 927–934.
- [14] M. Mostafavi, D.J. Smith, M.J. Pavier, *Fatigue Fract. Eng. Mater. Struct.* 33 (2010) 724–739.
- [15] M. Mostafavi, D.J. Smith, M.J. Pavier, *Eng. Fract. Mech.* 78 (2011) 1705–1716.
- [16] DaVis, *User's Manual*, LaVision GmbH., Gottingen, 2009.
- [17] M.A. Sutton, S.R. McNeill, J.D. Helm, Y.J. Chao, *Top. Appl. Phys.* 77 (2000) 323–372.
- [18] BS-EN-843-2, *British Standards Institute; BS EN 843-2:2007; Advanced Technical Ceramics—Part 2: Determination of Young's Modulus, Shear Modulus and Poisson's Ratio* BSI, 2007.
- [19] T.L. Panontin, A. Makino, J.F. Williams, *Eng. Fract. Mech.* 67 (2000) 293–301.
- [20] Y.Y. Wang, H.S. Reemsnyder, M.T. Kirk, *Influence equations for fracture toughness testing: numerical analysis and experimental verification*, in: J.H. Underwood, B.D. Macdonald, M.R. Mitchell (Eds.), *Fatigue and Fracture Mechanics*, ASTM, ASTM Special Technical Publication (STP 1321), Ann Arbor, MI, 1997, pp. 469–484.
- [21] ABAQUS, *User's Manual*, ABAQUS Inc., Providence, Rhode Island, Version 6.9, 2009.
- [22] G.B. Sinclair, *Int. J. Fract.* 28 (1985) 3–16.
- [23] F.Z. Li, C.F. Shih, A. Needleman, *Eng. Fract. Mech.* 21 (1985) 405–421.
- [24] W. Brocks, I. Scheider, *Numerical aspects of the path-dependence of the J-integral in incremental plasticity—How to calculate reliable J-values in FE analyses*, *Inst. Werkstofforsch.* (2001).
- [25] T.J. Marrow, A.D. Hodgkins, M.R. Joyce, B.J. Marsden, *Eng. Mater.* 1 (2006) 167–170.
- [26] G.C. Sih, P.C. Paris, G.R. Irwin, *Int. J. Fract.* 1 (1965) 189–203.
- [27] J.C. Newman, *Stress analysis of the compact specimen including the effects of pin loading*, in: G.R. Irwin (Ed.), *Fracture Analysis: Proceedings of the 1973 National Symposium on Fracture Mechanics (ASTM STP 560)*, American Society for Testing and Materials, Philadelphia, 1974, pp. 105–121.
- [28] R6, *Assessment of the Integrity of Structures Containing Defects*, British Energy, 2001.
- [29] C.E. Turner, O. Kolednik, *Fatigue Fract. Eng. Mater. Struct.* 17 (1994) 1089–1107.
- [30] O. Kolednik, M. Albrecht, M. Berchthaler, H. Germ, R. Pippan, F. Riemelmoser, J. Stampfl, J. Wei, *Acta Mater.* 44 (1996) 3307–3319.
- [31] V.P. Naumenko, S.V. Lenzion, I.V. Limansky, *Open Mech. Eng. J.* 2 (2008) 40–59.
- [32] P.J. Heard, M.R. Wootton, R. Moskvic, P.E.J. Flewitt, *J. Nucl. Mater.* 401 (2010).
- [33] T.H. Becker, R.B. Tait, in: *12th International Conference on Fracture*, Ottawa, Canada, 2009.
- [34] M.A. Sutton, X. Deng, F. Ma, J.C. Newman, M. James, *Int. J. Solids Struct.* 37 (2000) 3591–3618.
- [35] B. Moran, C.F. Shih, *Int. J. Fract.* 35 (1987) 295–310.
- [36] X. Chen, in: *Department of Civil Engineering, University of Maryland, College Park*, 2005.
- [37] J.W. Hutchinson, *J. Appl. Mech.* 50 (1983) 1042–1051.
- [38] P.F. Thomason, *Int. J. Fract.* 44 (1990) 259–281.
- [39] V. Vitek, G.G. Chell, *Mater. Sci. Eng.* 27 (1977) 209–215.
- [40] F. Mecklenburg, J.A. Joyce, P. Albrecht, *Separation of energies in elastic-plastic fracture*, in: J.D. Landes, A. Saxena, J.G. Merkle (Eds.), *Nonlinear Fracture Mechanics*, vol. II, *Elastic–Plastic Fracture*, ASTM STP, 1989, p. 995.
- [41] J.D.G. Sumpter, *Eng. Fract. Mech.* 71 (2004) 17–37.
- [42] Y.Y. Wang, D.M. Parks, *Limits of J–T characterization of elastic-plastic crack tip fields*, in: M.T. Kirk, A. Bakker (Eds.), *Constraint Effects in Fracture Theory and Applications: Second Volume*, ASTM STP 1244, American Society for Testing and Materials, Philadelphia, 1995.
- [43] M. Mostafavi, T.J. Marrow, *Fatigue Fract. Eng. Mater. Struct.* 35 (2012) 695–707.
- [44] A. Hillerborg, M. Modeer, P.E. Petersson, *Cem. Concr. Res.* 6 (1976) 773–782.
- [45] D.N. Jadhav, S.K. Maiti, *Nucl. Eng. Des.* 240 (2010) 713–721.
- [46] V. Tvergaard, J.W. Hutchinson, *J. Mech. Phys. Solids* 40 (1992) 1377–1397.
- [47] H.L. Yuan, A. Cornec, *J. Eng. Mater. Technol.*, 118, *Trans. ASME*, 1996 192–200.
- [48] A. Cornec, I. Scheider, K.H. Schwalbe, *Eng. Fract. Mech.* 70 (2003) 1963–1987.
- [49] K.H. Schwalbe, I. Scheider, A. Cornec, *THE SIAM Method for Applying Cohesive Models to the Damage Behaviour of Engineering Materials and Structures*, GKSS - Forschungszentrum Geesthacht GmbH (2009).
- [50] A. Banerjee, R. Manivasagam, *Eng. Fract. Mech.* 76 (2009) 1761–1770.
- [51] P.R. Goggin, W.N. Reynolds, *Philos. Mag.* 16 (1967) 317–330.